Synthesis, elasticity and spin state of an intermediate MgSiO₃-FeAlO₃ bridgmanite: Implications for iron in Earth's lower mantle

Feng Zhu[1,2*], Jiachao Liu[1,3], Xiaojing Lai[2,4], Yuming Xiao[5], Vitali Prakapenka[6], Wenli Bi[7,8,9], E. Ercan Alp[7], Przemyslaw Dera[2], Bin Chen[2], Jie Li[1*]

[1]Earth and Environmental Sciences, University of Michigan, Ann Arbor, MI 48109, USA.

[2]Hawaiʻi Institute of Geophysics and Planetology, University of Hawaiʻi at Mānoa, Honolulu, HI 96822, USA.

[3]Earth and Environmental Sciences, Michigan State University, East Lansing, MI 48824, USA.

[4]Gemmological Institute, China University of Geosciences, Wuhan, Hubei, 430074, China.

[5]HPCAT, Advanced Photon Source, Argonne National Laboratory, Argonne, IL 60439, USA.

[6]Center for Advanced Radiation Sources, University of Chicago, Argonne, IL 60437, USA.

[7]Advanced Photon Source, Argonne National Laboratory, Argonne, IL 60439, USA.

[8]Department of Geology, University of Illinois at Urbana-Champaign, Urbana, IL 61801, USA.

[9]Department of Physics, University of Alabama at Birmingham, Birmingham, AL 35294, USA.

Corresponding authors: Feng Zhu (zhufeng@hawaii.edu); Jie Li (jackieli@umich.edu)

Key Points:

- Bridgmanite may contain 50% trivalent cations through Fe^{3+}-Al^{3+} coupled substitution
- The bulk sound velocity of $(Mg_{0.5}Fe^{3+}_{0.5})(Al_{0.5}Si_{0.5})O_3$ bridgmanite is 7.7% lower than $MgSiO_3$
- Through Fe-Al cation exchange, Fe^{3+} in $(Mg_{0.5}Fe^{3+}_{0.5})(Al_{0.5}Si_{0.5})O_3$ bridgmanite undergoes gradual spin transition at lower mantle conditions

Abstract

Fe-Al-bearing bridgmanite may be the dominant host for ferric iron in Earth's lower mantle. Here we report the synthesis of $(Mg_{0.5}Fe^{3+}_{0.5})(Al_{0.5}Si_{0.5})O_3$ bridgmanite (FA50) with the highest Fe^{3+}-Al^{3+} coupled substitution known to date. X-ray diffraction measurements showed that at ambient conditions the FA50 adopted the $LiNbO_3$ structure. Upon compression at room temperature to 18 GPa, it transformed back into the bridgmanite structure, which remained stable up to 102 GPa and 2600 K. Fitting Birch-Murnaghan equation of state of FA50 bridgmanite yields $V_0 = 172.1(4)$ Å^3, $K_0 = 229(4)$ GPa with $K_0' = 4$(fixed). The calculated bulk sound velocity of the FA50 bridgmanite is ~7.7% lower than $MgSiO_3$ bridgmanite, mainly because the presence of ferric iron increases the unit-cell mass by 15.5%. This difference likely represents the upper limit of sound velocity anomaly introduced by Fe^{3+}-Al^{3+} substitution. X-ray emission and synchrotron Mössbauer spectroscopy measurements showed that after laser annealing ~6% of Fe^{3+} cations exchanged with Al^{3+} and underwent the high-spin to low-spin transition at 59 GPa. The low-spin proportion of Fe^{3+} increased gradually with pressure and reached 17-31% at 80 GPa. Since the cation exchange and spin transition in this Fe^{3+}-Al^{3+}-enriched bridgmanite do not cause resolvable unit-cell volume reduction, and the increase of low-spin Fe^{3+} fraction with pressure occurs gradually, the spin transition would not produce a distinct seismic signature in the lower mantle. However, it may influence iron partitioning and isotopic fractionation, thus introducing chemical heterogeneity in the lower mantle.

Plain Language Summary

Fe-Al-bearing bridgmanite may be the dominant mineral in the lower mantle, which occupies more than half of Earth's volume. A subject of much debate is whether spin transition of Fe in bridgmanite produces an observable influence on the physics and chemistry of the lower mantle. In this study, we synthesized a new $(Mg_{0.5}Fe^{3+}_{0.5})(Al_{0.5}Si_{0.5})O_3$ bridgmanite with the highest Fe^{3+}-Al^{3+} coupled substitution known to date. We studied its structure, elasticity, and spin state by multiple experimental and theoretical methods. The high Fe content allowed us to better resolve a pressure-induced spin transition of Fe^{3+} caused by Fe-Al cation exchange at high temperature. Our results suggest that the spin transition is enabled by cation exchange but has a minor effect on the seismic velocity, although it may introduce chemical heterogeneity in the lower mantle. Our study helps resolve existing discrepancies on the nature of spin transition of Fe-Al bridgmanite and its influence on the physics and chemistry of the lower mantle.

1 Introduction

Bridgmanite is the dominant phase in the Earth's lower mantle (Tschauner et al., 2014). It has an ABX_3-type perovskite structure, consisting of eight corner-sharing BX_6 octahedra with a larger A cation caged in the center AX_{8-12} pseudo-dodecahedral site. The main composition of bridgmanite is $MgSiO_3$, but it can also accommodate a considerable amount of Fe^{2+} in its A site and coupled Fe^{3+} and Al^{3+} in its A and B sites for charge balance (Andrault et al., 2001; Boffa Ballaran et al., 2012; Glazyrin et al., 2014; Nishio-Hamane et al., 2008; Nishio-Hamane et al., 2005). Therefore its actual chemical composition in the Earth's lower mantle can vary within the formula $(Mg,Fe^{2+},Fe^{3+},Al)(Si,Al,Fe^{3+})O_3$ depending on different bulk composition, pressure (P), temperature (T) and oxygen fugacity (f_{O2}). Frost et al. (2004) showed that Fe^{2+} in bridgmanite underwent a self-disproportionation at lower mantle P-T conditions, elevating the concentration of Fe^{3+} in bridgmanite. Since most peridotitic and basaltic sources have a higher than unity Al/Fe

66　ratio (Mohn & Trønnes, 2016), and Fe^{3+}-Al^{3+} coupled substitution is the favored mechanism to
67　incorporate trivalent cations into bridgmanite (Andrault et al., 2001; Mohn & Trønnes, 2016;
68　Nishio-Hamane et al., 2005), the Fe-Al bridgmanite can be a dominant phase to host Fe and Al in
69　the lower mantle (Wang et al., 2015).

70　　　　As the only major element with variable valence and potential magnetic transition in
71　bridgmanite, iron plays a key role on its elastic and electrical properties. It may also influence
72　element partitioning and isotopic fractionation in the Earth's mantle (Badro, 2014; Lin et al.,
73　2013). Whether bridgmanite undergoes any spin transition under Earth's lower mantle
74　conditions, however, is a question hanging for decades. The Fe^{2+} can only occupy A site in
75　perovskite structure. It was suggested to undergo a high-spin (HS) to low-spin (LS), or HS to
76　intermediate-spin (IS) transition in earlier studies, but recent researches demonstrated that Fe^{2+}
77　shows no spin transition in A site up to at least 120 GPa (reviewed by Badro (2014)). The Fe^{3+} in
78　A site also has no spin transition within the mantle pressure range, but the Fe^{3+} in B site was
79　reported to transform to LS-state at 15-50 GPa in multiple studies (Catalli et al., 2010; Fu et al.,
80　2018; Liu et al., 2018; Mao et al., 2015; Okuda et al., 2019). Some studies further argued that HS
81　Fe^{3+} can undergo a cation exchange with Al^{3+} in B site at ~40-80 GPa and high temperature, in
82　which B-site Fe^{3+} will subsequently transform into LS-state as discussed above (Catalli et al.,
83　2011; Fujino et al., 2012; Kupenko et al., 2015), but the others did not observe this cation
84　exchange and spin transition (Dubrovinsky et al., 2010; Glazyrin et al., 2014; Potapkin et al.,
85　2013). Theoretical calculations also predicted the Fe-Al cation exchange to be energetically
86　unfavorable due to the large Bader radius of both HS and LS Fe^{3+} (Mohn & Trønnes, 2016). To
87　date, the controversy on the cation exchange - spin transition hypothesis in (Fe,Al)-bearing
88　bridgmanite has not been fully resolved yet.

89　　　　In this study, we synthesized a new bridgmanite sample with the composition
90　$(Mg_{0.47-0.50}Fe_{0.52})(Al_{0.46-0.47}Si_{0.51-0.55})O_3$, hereafter referred to FA50, and studied its structure,
91　elastic and electronic properties by X-ray diffraction (XRD), X-ray emission spectroscopy (XES)
92　and synchrotron Mössbauer spectroscopy (SMS) experiments and DFT calculations. With the
93　highest fraction of Fe-Al substitution, we aim to better resolve the potential cation exchange and
94　spin transition under high pressure and high temperature and investigate the influence of Fe-Al
95　incorporation in bridgmanite on the physics and chemistry of the lower mantle.

96　**2 Materials and Methods**

97　　　　2.1 Multi-anvil apparatus synthesis and characterization

98　　　　The synthesis was conducted using the 1000-ton multi-anvil apparatus (MA) at the
99　University of Michigan. The starting materials were a mixture of MgO, SiO_2, Fe_2O_3, Al_2O_3 with
100　2:2:1:1 molar ratio. In the synthesis of ^{57}Fe-enriched sample, half of the Fe_2O_3 was replaced by
101　$^{57}Fe_2O_3$. The mixture was heated at 1073 K for 8 hrs to remove the moisture and structure water
102　before sample loading. The COMPRES 8/3 cell assemblies were used in the synthesis (K. D.
103　Leinenweber et al., 2012). The sample was loaded in a platinum capsule and kept at 24 GPa and
104　1873 K for 10 hrs before quenching to room temperature and then decompressed to 1 bar. The
105　recovered product was examined by JOEL-7800FLV Scanning Electron Microprobe (SEM) and
106　SX-100 Electron Microprobe Analysis (EPMA) at the Electron Microbeam Analysis Laboratory
107　(EMAL) of the University of Michigan. The accelerating voltage and beam current were set at 15
108　kV and 10 nA. The product consists of mainly $(Mg_{0.5}Fe_{0.5})(Al_{0.5}Si_{0.5})O_3$ (FA50, exact formula

109    $(Mg_{0.50}Fe_{0.52})(Al_{0.47}Si_{0.51})O_3$ and $(Mg_{0.47}Fe_{0.52})(Al_{0.46}Si_{0.55})O_3$ in two independent runs), with

110   minor excess Al_2O_3 and SiO_2, and a coexisting Si-deficient oxide $Mg_{1.47}Fe_{2.46}Al_{1.11}Si_{0.12}O_7$,

111   hereafter referred to MFA (Figure S1 and Table S1).

112   2.2 Diamond anvil cell experiments

113   Diamond anvil cells (DAC) with 150 μm and 300 μm diameter diamond culets were

114   employed in the synchrotron XRD experiment up to 102 GPa, and XES and SMS experiments up

115   to 80 GPa, respectively. Rhenium gasket was used for the XRD experiment and beryllium gasket

116   was used for the XES and SMS experiments. XES and SMS data were collected on the same

117   sample. The gaskets were pre-indented to ~30 μm thickness. Holes of 90 μm for 150 μm culet

118   and 150 μm for 300 μm culet were drilled by the laser-drilling system at HPCAT of Advanced

119   Photon Source (APS), Argonne National Lab (ANL).

120   The XRD experiment was conducted at beamline 13-ID-D at APS, ANL. Two sample

121   grains with ~30 μm diameter and ~15 μm thickness were picked from the MA synthesis product

122   and loaded into the sample chamber. Au powder was dispersed into the sample chamber as the

123   pressure calibrant (Fei et al., 2007). Neon gas was loaded as the pressure medium and thermal

124   insulator using the COMPRES/GSECARS gas loading system at APS, ANL. The incident X-ray

125   beam size was ~3 μm in diameter and the wavelength was 0.3344 Å. A flat-top double-sided

126   laser-heating system, with the beam spot focused to 30-40 μm, was used to reach high

127   temperatures (Prakapenka et al., 2008). We scan-heated the sample continuously to avoid

128   creating large temperature gradient inside the sample. The two sample grains were first

129   compressed to ~27 GPa and laser-annealed at 1600-1800 K for 10 mins until the XRD showed

130   the sample was fully converted to bridgmanite polycrystalline phase. One sample grain was then

131   further compressed and laser-annealed each time after compression to facilitate the potential

132   phase transition and cation exchange. XRD patterns were collected twice before and after laser-

133   annealing. The other sample grain was compressed simultaneously without laser-annealing for

134   comparison. All XRD patterns used for lattice refinement were collected by applying a ±10°

135   rotation wide scan to improve the number and quality of the peaks. The Au peaks appear

136   together with the sample peaks in the XRD patterns so the pressure deviation between sample

137   and pressure marker was minimized. Dioptas (Prescher & Prakapenka, 2015), GSAS (Toby,

138   2001) and PDIndexer (Seto et al., 2010) software were used to integrate and process the XRD

139   data. The lattice parameters were fitted by a Le-Bail method. The sample peaks overlapped with

140   gold or neon peaks were excluded from the fitting.

141   The XES experiment was conducted at beamline 16-ID-D at APS, ANL. A sample with

142   ~40 μm diameter and ~15 μm thickness was directly loaded into the sample chamber. Silicone

143   oil was used as the pressure medium, and the edge of Raman peak from diamond culet was used

144   for the pressure calibration (Akahama & Kawamura, 2006). The incident X-ray beam size was

145   5×7 μm^2, and the beam energy is 11.3 keV with a bandwidth of ~1 eV. Fe K_β emission was

146   selected by silicon analyzer and reflected to a silicon detector with an energy step of about 0.3

147   eV. Each spectrum took ~40 min and 1–3 spectra were taken to accumulate at least 30,000

148   counts at the Fe K_β main peak at each pressure. The sample was laser annealed at 1300-2100 K

149   for 15-35 mins at 59, 75 and 80 GPa to facilitate the potential phase transition and cation

150   exchange at 13-ID-D, using the same procedure as that in XRD experiments. The time-domain

151   SMS measurements were performed on the same sample in XES experiments at beamline 3-ID-

152   B at APS, ANL. The time window of SMS with effective statistics was extended to 250 ns in

153   hybrid mode, providing better constraint on the hyperfine parameter. The incident X-ray beam
154   size was ~20×20 μm^2. Each spectrum was collected for ~12 h. The CONUSS package was used
155   for the data processing (Sturhahn, 2000).

156   2.3 Density functional theory calculation

157   Density functional theory (DFT) calculation was performed using the Vienna *Ab initio*
158   Simulation Package (VASP) in the MedeA software (Kresse & Furthmüller, 1996). Exchange
159   and correlation were treated using PBE-GGA pseudopotential. The energy cut-off was set to 520
160   eV. The convergence criteria for the self-consistency loop was set to 10^{-5} eV. The k-points grid
161   was set to 6×6×4 for original bridgmanite lattice and was scaled down by ratio when building the
162   supercells. Spin-polarization was included for Fe atom. The $MgSiO_3$ bridgmanite structure was
163   used as the prototype and eleven different types of Fe-Al substitution configurations were
164   selected to search for the most energetically stable structure of $(Mg_{0.5}Fe_{0.5})(Al_{0.5}Si_{0.5})O_3$
165   bridgmanite.

3 Results and Discussions

167   3.1 $LiNbO_3$ – bridgmanite phase transition

168   The quenched product FA50 from the MA experiments can be initially indexed as a
169   corundum-type structure at ambient pressure (Figure 1). It transformed into bridgmanite at 18.8
170   GPa. The bridgmanite phase remained stable from 26.8 to 102.2 GPa after laser-annealing
171   treatment (Figure 1b). The transition to bridgmanite occurred without heating and at ~5 GPa
172   lower than that for pure $MgSiO_3$. Since the sample was synthesized in MA at 24 GPa which
173   exceeds the transition pressure, the corundum-type phase may have formed retrogressively
174   during decompression. Both the forward and reverse transitions can proceed without heating,
175   implying a low kinetic barrier between the two phases. The low kinetic barrier may be explained
176   by the structures of the perovskite and $LiNbO_3$-type phases, which are related through the
177   rotation of the BX_6 octahedra without breaking B-X bonds (Ross et al., 1989). The *c/a* ratio of
178   the quenched sample is 2.67, consistent with the expected value of ~2.63-2.69 for $LiNbO_3$-type
179   ordering (Abrahams & Marsh, 1986; Ko & Prewitt, 1988; K. Leinenweber et al., 1995) and
180   smaller than those of the corundum prototype at ~2.73 (Blake et al., 1966; Yim & Paff, 1974) or
181   ilmenite-type ordering at ~2.77-2.87 (Horiuchi et al., 1982; Kidoh et al., 1984; Wechsler &
182   Prewitt, 1984). The $LiNbO_3$-type phase is completely ordered between the A and B sites, each
183   consisting of a corner-sharing octahedral framework. One set of corner-sharing framework is
184   fully occupied by Si and Al cations, which rotates to the BX_6 corner-sharing framework of
185   bridgmanite; the other set is occupied by Mg and Fe cations, which displaces to the pseudo-
186   dodecahedral A site in bridgmanite upon compression.

187   In the FA50 bridgmanite, both A site and B site are occupied by two cations instead of
188   one. To search for the most stable ordering of Mg/Fe in A site and Si/Al in B site, we performed
189   DFT calculations on 11 structures of $(Mg_{0.5}Fe_{0.5})(Al_{0.5}Si_{0.5})O_3$ with different cation arrangements
190   at 0 K. The three energetically favored structures share the same type of Si/Al ordering in B site,
191   in which Si and Al atoms alternate in all axial directions. With this B-site framework, an altered
192   Mg and Si sheet arrangement in *ac* plane along *b* direction is most energetically favorable, while
193   the strip arrangement along *b* direction is the closest competitor with 33 meV higher in internal
194   energy (Figure 2). The $LiNbO_3$-type phase as a retrogressive product should share the same
195   cation framework of bridgmanite. It is worth noting that the complete cation ordering inside A

196 and B site can be disrupted by the elevated temperature, thus further experiments are still needed
197 to testify these predicted orderings.

198   3.2 Equation of state and spin transition

199   The sample grains were heated to 1600-1800 K for 10 mins at ~27 GPa to release stress
200 and facilitate the formation of bridgmanite from $LiNbO_3$ phase. The two bridgmanite samples
201 were then compressed to ~102 GPa with a 2-7 GPa pressure interval. Previous studies showed
202 that due to kinetic barrier Fe-Al exchange only occurred at high temperature (Catalli et al., 2011;
203 Fujino et al., 2012; Kupenko et al., 2015). Therefore, we laser-annealed sample 1 at 1600-2200
204 K for 10-25 min each time after compression to facilitate cation exchange and phase transition
205 (Figure S2). This sample should always adopt the stable cation ordering at high pressure and
206 high temperature conditions at the whole pressure range. Two XRD patterns were collected after
207 each compression, one before and the other after the laser-annealing for the laser-annealed
208 sample (gray and red squares in Fig. 3). The pressure after laser-annealing was higher than that
209 before laser-heating, because the pressure was still slowly increasing during heating. We tried to
210 fit the unit-cell volume as a function of pressure by the second-order Birch-Murnaghan equation
211 of state (BM-EoS). Fitting only the data after laser-annealing (red squares in Fig. 3) yields $V_0 =$
212 172.0(7) $Å^3$, $K_0 = 230(6)$ GPa with $K_0' = 4$(fixed), while fitting both the data before and after
213 laser-annealing (gray and red squares in Fig. 3) yields $V_0 = 172.1(4)$ $Å^3$, $K_0 = 229(4)$ GPa with
214 $K_0' = 4$(fixed). The two EoSs are almost identical within uncertainty, indicating laser-annealing
215 at each pressure points did not introduce visible volume collapse from potential cation exchange
216 and spin transition. Therefore, the second EoS with a denser data coverage and smaller
217 uncertainties was used to represent the EoS for thermodynamically stable structure and ordering
218 of FA50 sample. The slope of normalized stress – Eulerian strain (*F-f*) fitting is almost flat,
219 indicating the validity of fixing K_0' to 4.

220   Sample 2 was only cold compressed thus no cation exchange and spin transition were
221 expected, and it served as a reference for the initial cation ordering. This sample has a similar or
222 slightly lower volume at the whole pressure range with the laser-annealed sample. Its EoS
223 parameters $V_0 = 170.7(3)$ $Å^3$, $K_0 = 240(3)$ GPa with $K_0' = 4$(fixed) confirmed this observation.
224 DFT calculations give EoS parameters of $V_0 = 176.5(5)$ A^3, $K_0 = 212(12)$ GPa and $K_0' = 3.97(33)$
225 from energy-volume fitting, in which the Fe^{3+} is at A-site and HS, consistent with the EoS of
226 sample 2 with a typical overestimation of V_0 and underestimate of K_0. If sample 1 has a
227 continuous cation exchange and spin transition along with the increased pressure, it should have
228 a lower volume and softened K_0 compared with those of sample 2. However, the volumes do not
229 show the trend as expectation, suggesting that even if there is any cation exchange and spin
230 transition in sample 1, it does not introduce visible volume collapse compared with its original
231 state. The bulk modulus of sample 1 is lower than sample 2 as expected, but the difference is
232 small and not conclusive enough to determine any transition considering the uncertainty level
233 indicated by the inverse trend in volume. Overall, comparing these two samples could not
234 distinguish any pressure-induced cation exchange and spin transition as suggested in other FA
235 bridgmanite (Catalli et al., 2011; Fujino et al., 2012; Kupenko et al., 2015), indicating either
236 there is no cation exchange, or the cation exchange and subsequent spin transition does not
237 introduce resolvable difference by XRD method.

238   The FA50 bridgmanite has a larger unit-cell volume than $MgSiO_3$ and other Fe,Al-
239 bearing bridgmanite samples with lower Fe-Al contents, due to the large ionic size of Fe^{3+} and

240   Al^{3+} (Andrault et al., 2001; Boffa Ballaran et al., 2012; Nishio-Hamane et al., 2008). Its unit-cell
241   volume is smaller than the $(Mg_{0.46}Fe_{0.53})(Fe_{0.51}Si_{0.49})O_3$ (FF50) bridgmanite (Liu et al., 2018),
242   which indicates Fe^{3+}(HS) > Fe^{3+}(LS) > Al^{3+} in B site. This relation is consistent with the ionic
243   radius at ambient pressure (Shannon, 1976) The gap between FA50 and LS-state FF50
244   bridgmanite decreases with pressure, indicating Fe^{3+}(LS) is more compressible than Al^{3+} at high
245   pressure. When comparing these Fe-Al substituted bridgmanites at $K_0' = \sim4$, the unit-cell
246   volumes exhibit a quasi-linear relation with the fraction of Fe-Al substitution (Figure S3). The
247   bulk moduli have a negative correlation to the unit-cell volumes (Table S2) (Andrault et al.,
248   2001; Boffa Ballaran et al., 2012; Liu et al., 2018; Nishio-Hamane et al., 2008) except a small
249   anomaly between $MgSiO_3$ (Boffa Ballaran et al., 2012) and FA5 (Andrault et al., 2001) within
250   uncertainty, consistent with that the larger ion is more compressible.

251   To further examine spin transition, we performed XES and SMS measurements, which
252   are more sensitive probes for the electronic configuration than XRD, on the FA50 bridgmanite
253   (Figure 4 &5). The sample was compressed from 18 to 80 GPa and laser-heated at three
254   pressures of 59, 75 and 80 GPa. In XES spectra, the area depression of the satellite peak around
255   7044 eV was used to quantify the fraction of LS Fe^{3+} in B site. The area difference was
256   calculated by subtracting the spectrum of LS standard from the measured ones, and the spectrum
257   at 18 GPa is set as HS standard. The intensity relative difference (IRD) and intensity absolute
258   difference (IAD) methods were both applied to calculate the area difference (Figure 4b) (Mao et
259   al., 2014). Before laser heating at 18-54 GPa, the area of the satellite peaks remains similar to HS
260   standard, indicating no spin transition. After the first laser annealing at 59 GPa, the peak area
261   was depressed by ~6%, indicating ~6% Fe^{3+} transformed into LS-state (Fig. 2b). It also implies
262   the same fraction of Fe^{3+} exchanged into B site. The peak area was further diminished at 75 GPa
263   and 80 GPa where laser-annealing treatment was applied. The good correlation between peak
264   area and laser-annealing treatment indicates that high temperature is necessary to overcome the
265   kinetic barrier during cation-exchange induced spin transition. The increased fraction of cation
266   exchange with pressure indicates that the transition could happen in a wide pressure range, where
267   the LS-state B-site Fe^{3+} continuously increase with depth (Figure 4b). At 80 GPa after laser
268   annealing, the fraction of LS Fe^{3+} increased to 17-29% from IRD and IAD methods, respectively,
269   implying that the fraction of Fe^{3+} HS-LS transition increases with pressure. The 59 GPa pressure
270   point thus only gave an upper limit of the initiation pressure of the cation exchange and spin
271   transition, while the transition could initiate at lower pressure if been heated. If extrapolated from
272   the pressure – HS fraction of Fe^{3+} at 59, 75 and 80 GPa, the initiation pressure was roughly
273   estimated at ~47 GPa, but the uncertainty is extremely large thus further investigation is needed
274   with denser pressure coverage. In addition, we collected two SMS spectra at 35 GPa and 80 GPa
275   on the same sample before and after laser annealing, which confirmed the magnetic transition
276   (Figure 5). The spectrum at 35 GPa can be well explained by one HS Fe^{3+} site, while the
277   spectrum at 80 GPa needs at least two Fe^{3+} sites for a satisfactory fitting. The fitted Quadrupole
278   Splitting (QS) of Fe^{3+} was consistent with those in previous studies (Lin et al., 2012; Liu et al.,
279   2015). The LS proportion is 31%, consistent with XES measurement within uncertainties. The
280   observed cation-exchange-induced spin transition coincides with several previous studies (Catalli
281   et al., 2011; Fujino et al., 2012; Kupenko et al., 2015) but opposites to the others (Dubrovinsky
282   et al., 2010; Glazyrin et al., 2014; Potapkin et al., 2013). The absence of observation of spin
283   transition in these previous studies may be resulted from the kinetic barrier of cation exchange,
284   or the low signal due to low Fe^{3+} concentration.

285   The limited fraction of cation exchange and spin transition also explains the absence of
286 volume collapse in XRD results. The volume reduction associated with full transformation of B
287 site Fe^{3+} in $(Mg_{0.5}Fe_{0.5})(Fe_{0.5}Si_{0.5})O_3$ into the LS-state is estimated at ~0.5% (Liu et al., 2018). In
288 our sample, if 20% of the Fe^{3+} enters the B-site after laser annealing, the transformation of
289 $(Mg_{0.5}Fe_{0.4}Al_{0.1})(Fe_{0.1}Al_{0.4}Si_{0.5})O_3$ to the LS-state at ~80 GPa would produce ~0.1% volume
290 reduction (~0.14 $Å^3$), well below the uncertainty level of volume refinement. The volume
291 reduction would be even smaller in the Earth's mantle, which typically has much lower Fe-Al
292 contents (Boffa Ballaran et al., 2012; Glazyrin et al., 2014).

293   3.3 Bulk sound velocity

294   Although the spin transition in Fe-Al bridgmanite is likely seismically invisible, the
295 compositional difference between Fe-Al bridgmanite and $MgSiO_3$ bridgmanite results in
296 significant contrast in their density and compressibility, which leads to the difference in bulk
297 sound velocity:

298 $$v_\Phi = \sqrt{K/\rho} = \sqrt{KV/M} \quad (1)$$

299 where ρ is density, M and V are the unit-cell mass and volume. Figure 6 plotted v_Φ of different
300 bridgmanites as a function of pressure. The v_Φ can also be calculated from the direct sound
301 velocity measurement by

302 $$v_\Phi = \sqrt{v_p{}^2 - \frac{4}{3}v_s{}^2} \quad (2)$$

303 where v_p is the compressional wave velocity and v_s is the shear wave velocity.

304   The v_Φ decreases systematically with increased Fe-Al content in these bridgmanites,
305 because the differences of v_Φ mainly come from the unit-cell mass difference introduced by Fe
306 substitution. The K and V of these bridgmanites are anti-correlated with each other as discussed
307 above, making the KV term close in value for different bridgmanite and the M the dominant
308 factor for the difference in v_Φ. For example, at 130 GPa $MgSiO_3$ and FA50 have only -1.6%
309 difference in KV, but a constant 15.5% difference in M; The v_Φ of FA50 is about 7.7% smaller
310 than that of $MgSiO_3$ bridgmanite and this difference is dominated by the difference in M (Figure
311 6). Thus, from the mass difference, FA50 might represent the highest sound velocity variation
312 introduced by the coupled Fe-Al substitution. v_Φ of FF50 is ~16.4% smaller than that of $MgSiO_3$
313 bridgmanite at 130 GPa (Liu et al., 2018), which means substituting 50% Fe in B site further
314 reduce bulk sound velocity by ~8.7%, quite similar to substituting 50% Fe in A site. Therefore,
315 the incorporation of Fe^{3+} into either/both sites decreases v_Φ equally by ~8.2% for each 0.25
316 $Fe^{3+}/(Fe^{3+}+Mg+Si+Al)$, at core-mantle boundary pressure, which can serve as a criterion on
317 detecting Fe-enriched region in lower mantle. The similar volume deduction for A and B sites
318 also implies that a significant sound velocity discontinuity is not expected during cation
319 exchange.

320   When comparing the v_Φ derived from sound velocity measurement with the v_Φ calculated
321 from EoS parameters of similar compositions, the F6A4 and F12A11 composition matches well
322 with the range defined by FA5 and FA15 (Fu et al., 2019), but the FA10 showed a different
323 slope with increased pressure, mainly because the K' is 3.44(3), lower than those in other studies
324 (Kurnosov et al., 2017). It is still acceptable difference concerning the uncertainty range in sound
325 velocity measurements. Previous study also suggested that Fe^{3+}, if originally HS at B site, can

326 induce sound velocity discontinuity during spin transition due to the softening of bulk modulus K
327 (Fu et al., 2018). It is a different scenario for Fe-Al substituted bridgmanite where Fe^{3+} locate at
328 A site originally and the spin transition requires cation exchange. Although the Fe^{3+} turns to LS
329 state immediately after entering B-site at >15-50 GPa (Catalli et al., 2010; Fu et al., 2018; Liu et
330 al., 2018; Mao et al., 2015; Okuda et al., 2019), the cation exchange itself is a gradual process
331 with increased pressure throughout the whole lower mantle, which controls the fraction of LS
332 Fe^{3+}. Therefore, the changes resulted from the cation exchange and spin transition are distributed
333 into the whole lower mantle pressure, and a volume collapse or a bulk modulus softening is not
334 expected to occur within a narrow pressure range. We thus posit that the spin transition in Fe-Al
335 coupled bridgmanite does not cause a resolvable seismic discontinuity in Earth's mantle.

4 Implications and Conclusions

337 The prediction of Fe^{2+} disproportionation in bridgmanite (Frost et al., 2004) and the
338 positive correlation between Fe^{3+} and Al content in bridgmanite composition silicates from
339 diamond inclusions (McCammon et al., 1997) imply that Fe-Al coupled substitution may be a
340 major mechanism to accommodate Fe and Al in lower mantle. The solubility of Fe-Al in $MgSiO_3$
341 bridgmanite was suggested to have an upper limit since $FeAlO_3$ stabilizes as $Rh_2O_3(II)$ instead of
342 the perovskite structure (Nagai et al., 2005; Nishio-Hamane et al., 2005). Previous studies
343 reported the synthesis of a series of bridgmanites ranging from FA5 to FA40 (Andrault et al.,
344 2001; Boffa Ballaran et al., 2012; Nishio-Hamane et al., 2008). Here the synthesis of FA50
345 further elevates this upper limit of solubility to 50%, which may be an end member of this
346 bridgmanite series. More interestingly, FA50 may have different cation ordering from FA5-40
347 because FA50 can transform into a $LiNbO_3$-type phase reversibly, while FA5-FA40 did not have
348 similar transition and therefore always quenched as metastable bridgmanite. The difference may
349 be explained by the cation arrangement is more ordered in FA50, possibly due to the nearly 1:1
350 stoichiometric ratio of $MgSiO_3$ and $FeAlO_3$. Although complete ordering inside A and B sites is
351 unlikely at mantle temperatures, a more ordered cation arrangement may have lower entropy and
352 would be energetically favored under lower temperatures. Considering that both FA50 and
353 $MgSiO_3$ bridgmanite have lower entropy than the bridgmanites with intermediate composition,
354 the FA5-FA40 may decompose into FA50 and $MgSiO_3$ endmembers in order to minimize the
355 total free energy in low-temperature environments such as cold subducted slabs, which is also an
356 environment enriched with Fe^{3+}.

357 With the extreme iron enrichment in FA50 sample, we observed a gradual increase of the
358 fraction of B-site LS Fe^{3+} in Fe-Al coupled substitution bridgmanite due to Fe-Al cation
359 exchange. The spin transition, however, does not induce a sharp unit-cell volume reduction or
360 bulk modulus softening, thus may not be able to introduce detectable seismic anomaly at specific
361 pressure. It has also been suggested that Fe-Al coupled incorporation has very limited influence
362 on its electrical conductivity because it does not introduce site vacancy in bridgmanite that
363 enhances the conductivity (Potapkin et al., 2013; Sinmyo et al., 2014). The HS-LS transition in
364 FF50 only lowers the electrical conductivity by <0.3 log unit (Liu et al., 2018). Since the Fe-Al
365 site exchange in FA50 does not introduce additional defects from charge balance and the amount
366 of Fe^{3+} in B-site is less than FF50, the spin transition may also be difficult to be detected by
367 electromagnetic probes.

368 Isotopic fractionation of Fe in the lower mantle may be affected by the spin-transition of
369 Fe^{3+}- and Al^{3+}-bearing bridgmanite. When Fe^{3+} exchanges with Al^{3+} to enter the B site and

370 undergoes spin transition, the Fe-O bond shortens, and the coordination number decreases from 8
371 to 6. As the Fe-O bond in bridgmanite becomes stiffer with increasing depth, heavier Fe isotopes
372 may be favored in bridgmanite, as suggested by previous studies of isotopic fractionation
373 associated with spin transition in ferropericlase, Fe^{2+}-bearing bridgmanite and phase transition in
374 metallic iron alloys (Lai et al., 2017; Rustad & Yin, 2009). The increased fraction of B-site Fe^{3+}
375 with pressure may result in a chemical heterogeneity with depth. Further investigations are
376 needed from high-pressure experiments to test if the isotopic fractionation fits this prediction and
377 makes it a potential depth indicator for volcanic products and deep mantle diamond inclusions.

378   The B-site Fe^{3+} spin transition may also affect the iron partitioning between bridgmanite
379 and ferropericlase (Lin et al., 2013). However, the Fe in ferropericlase is dominantly Fe^{2+} and
380 therefore Fe-Mg re-partitioning between ferropericlase and Fe^{3+}-bearing bridgmanite would
381 require oxidizing or reducing source. In Earth's mantle, the metallic Fe^{0} produced from Fe^{2+}
382 disproportionation (Frost et al., 2004) can be a reducing source to partition more Fe into
383 ferropericlase during spin transition; conversely, the disproportionation reaction may produce
384 additional Fe^{3+} to enter bridgmanite, which serves as an additional oxidizing source. Therefore,
385 the cation exchange and spin transition can influence the Fe partitioning between Fe-Al
386 bridgmanite and ferropericlase in the Earth's mantle; meanwhile, this process may also slightly
387 change the redox state of lower mantle.

Acknowledgments

References

407 Abrahams, S., & Marsh, P. (1986). Defect structure dependence on composition in lithium niobate. *Acta*
408   *Crystallographica Section B: Structural Science, 42*(1), 61-68.
409 Akahama, Y., & Kawamura, H. (2006). Pressure calibration of diamond anvil Raman gauge to 310 GPa. *Journal of*
410   *Applied Physics, 100*(4), 043516.
411 Andrault, D., Bolfan-Casanova, N., & Guignot, N. (2001). Equation of state of lower mantle (Al, Fe)-MgSiO3
412   perovskite. *Earth and Planetary Science Letters, 193*(3-4), 501-508.
413 Badro, J. (2014). Spin transitions in mantle minerals. *Annual Review of Earth and Planetary Sciences, 42*, 231-248.

414 Blake, R., Hessevick, R., Zoltai, T., & Finger, L. W. (1966). Refinement of the hematite structure. *American*
415   *Mineralogist: Journal of Earth and Planetary Materials, 51*(1-2), 123-129.
416 Boffa Ballaran, T., Kurnosov, A., Glazyrin, K., Frost, D. J., Merlini, M., Hanfland, M., & Caracas, R. (2012). Effect
417   of chemistry on the compressibility of silicate perovskite in the lower mantle. *Earth and Planetary Science*
418   *Letters, 333*, 181-190.
419 Catalli, K., Shim, S.-H., Dera, P., Prakapenka, V. B., Zhao, J., Sturhahn, W., et al. (2011). Effects of the Fe3+ spin
420   transition on the properties of aluminous perovskite—New insights for lower-mantle seismic
421   heterogeneities. *Earth and Planetary Science Letters, 310*(3-4), 293-302.
422 Catalli, K., Shim, S.-H., Prakapenka, V. B., Zhao, J., Sturhahn, W., Chow, P., et al. (2010). Spin state of ferric iron
423   in MgSiO3 perovskite and its effect on elastic properties. *Earth and Planetary Science Letters, 289*(1-2),
424   68-75.
425 Dubrovinsky, L., Boffa-Ballaran, T., Glazyrin, K., Kurnosov, A., Frost, D., Merlini, M., et al. (2010). Single-crystal
426   X-ray diffraction at megabar pressures and temperatures of thousands of degrees. *High Pressure Research,*
427   *30*(4), 620-633.
428 Fei, Y., Ricolleau, A., Frank, M., Mibe, K., Shen, G., & Prakapenka, V. (2007). Toward an internally consistent
429   pressure scale. *Proceedings of the National Academy of Sciences, 104*(22), 9182-9186.
430 Frost, D. J., Liebske, C., Langenhorst, F., McCammon, C. A., Trønnes, R. G., & Rubie, D. C. (2004). Experimental
431   evidence for the existence of iron-rich metal in the Earth's lower mantle. *Nature, 428*(6981), 409-412.
432 Fu, S., Yang, J., Tsujino, N., Okuchi, T., Purevjav, N., & Lin, J.-F. (2019). Single-crystal elasticity of (Al, Fe)-
433   bearing bridgmanite and seismic shear wave radial anisotropy at the topmost lower mantle. *Earth and*
434   *Planetary Science Letters, 518*, 116-126.
435 Fu, S., Yang, J., Zhang, Y., Okuchi, T., McCammon, C., Kim, H. I., et al. (2018). Abnormal Elasticity of Fe‐
436   Bearing Bridgmanite in the Earth's Lower Mantle. *Geophysical Research Letters, 45*(10), 4725-4732.
437 Fujino, K., Nishio-Hamane, D., Seto, Y., Sata, N., Nagai, T., Shinmei, T., et al. (2012). Spin transition of ferric iron
438   in Al-bearing Mg–perovskite up to 200GPa and its implication for the lower mantle. *Earth and Planetary*
439   *Science Letters, 317*, 407-412.
440 Glazyrin, K., Ballaran, T. B., Frost, D., McCammon, C., Kantor, A., Merlini, M., et al. (2014). Magnesium silicate
441   perovskite and effect of iron oxidation state on its bulk sound velocity at the conditions of the lower mantle.
442   *Earth and Planetary Science Letters, 393*, 182-186.
443 Horiuchi, H., Hirano, M., Ito, E., & Matsui, Y. (1982). MgSiO3 (ilmenite-type): single crystal X-ray diffraction
444   study. *American Mineralogist, 67*(7-8), 788-793.
445 Kidoh, K., Tanaka, K., Marumo, F., & Takei, H. (1984). Electron density distribution in ilmenite‐type crystals. II.
446   Manganese (II) titanium (IV) trioxide. *Acta Crystallographica Section B: Structural Science, 40*(4), 329-
447   332.
448 Ko, J., & Prewitt, C. T. (1988). High-pressure phase transition in MnTiO 3 from the ilmenite to the LiNbO 3
449   structure. *Physics and Chemistry of Minerals, 15*(4), 355-362.
450 Kresse, G., & Furthmüller, J. (1996). Software VASP, vienna (1999). *Phys. Rev. B, 54*(11), 169.
451 Kupenko, I., McCammon, C., Sinmyo, R., Cerantola, V., Potapkin, V., Chumakov, A., et al. (2015). Oxidation state
452   of the lower mantle: In situ observations of the iron electronic configuration in bridgmanite at extreme
453   conditions. *Earth and Planetary Science Letters, 423*, 78-86.
454 Kurnosov, A., Marquardt, H., Frost, D., Ballaran, T. B., & Ziberna, L. (2017). Evidence for a Fe 3+-rich pyrolitic
455   lower mantle from (Al, Fe)-bearing bridgmanite elasticity data. *Nature, 543*(7646), 543.
456 Lai, X., Chen, B., Wang, J., Kono, Y., & Zhu, F. (2017). Polyamorphic Transformations in Fe‐Ni‐C Liquids:
457   Implications for Chemical Evolution of Terrestrial Planets. *Journal of Geophysical Research: Solid Earth,*
458   *122*(12), 9745-9754.
459 Leinenweber, K., Linton, J., Navrotsky, A., Fei, Y., & Parise, J. (1995). High-pressure perovskites on the join
460   CaTiO 3-FeTiO 3. *Physics and Chemistry of Minerals, 22*(4), 251-258.
461 Leinenweber, K. D., Tyburczy, J. A., Sharp, T. G., Soignard, E., Diedrich, T., Petuskey, W. B., et al. (2012). Cell
462   assemblies for reproducible multi-anvil experiments (the COMPRES assemblies). *American Mineralogist,*
463   *97*(2-3), 353-368.
464 Lin, J.-F., Alp, E. E., Mao, Z., Inoue, T., McCammon, C., Xiao, Y., et al. (2012). Electronic spin states of ferric and
465   ferrous iron in the lower-mantle silicate perovskite. *American Mineralogist, 97*(4), 592-597.
466 Lin, J.-F., Speziale, S., Mao, Z., & Marquardt, H. (2013). Effects of the electronic spin transitions of iron in lower
467   mantle minerals: Implications for deep mantle geophysics and geochemistry. *Reviews of Geophysics, 51*(2),
468   244-275.

469 Liu, J., Dorfman, S. M., Zhu, F., Li, J., Wang, Y., Zhang, D., et al. (2018). Valence and spin states of iron are
470   invisible in Earth's lower mantle. *Nature communications, 9*(1), 1284.
471 Liu, J., Mysen, B., Fei, Y., & Li, J. (2015). Recoil-free fractions of iron in aluminous bridgmanite from temperature-
472   dependent Mössbauer spectra. *American Mineralogist, 100*(8-9), 1978-1984.
473 Mao, Z., Lin, J.-F., Yang, J., Inoue, T., & Prakapenka, V. B. (2015). Effects of the Fe3+ spin transition on the
474   equation of state of bridgmanite. *Geophysical Research Letters, 42*(11), 4335-4342.
475 Mao, Z., Lin, J.-F., Yang, J., Wu, J., Watson, H. C., Xiao, Y., et al. (2014). Spin and valence states of iron in Al-
476   bearing silicate glass at high pressures studied by synchrotron Mössbauer and X-ray emission spectroscopy.
477   *American Mineralogist, 99*(2-3), 415-423.
478 McCammon, C., Hutchison, M., & Harris, J. (1997). Ferric iron content of mineral inclusions in diamonds from Sao
479   Luiz: A view into the lower mantle. *Science, 278*(5337), 434-436.
480 Mohn, C. E., & Trønnes, R. G. (2016). Iron spin state and site distribution in FeAlO3-bearing bridgmanite. *Earth
481   and Planetary Science Letters, 440*, 178-186.
482 Nagai, T., Hamane, D., Devi, P. S., Miyajima, N., Yagi, T., Yamanaka, T., & Fujino, K. (2005). A new polymorph
483   of FeAlO3 at high pressure. *The Journal of Physical Chemistry B, 109*(39), 18226-18229.
484 Nishio-Hamane, D., Seto, Y., Fujino, K., & Nagai, T. (2008). Effect of FeAlO3 incorporation into MgSiO3 on the
485   bulk modulus of perovskite. *Physics of the earth and planetary interiors, 166*(3-4), 219-225.

486 Nishio‐Hamane, D., Nagai, T., Fujino, K., Seto, Y., & Takafuji, N. (2005). Fe3+ and Al solubilities in MgSiO3
487   perovskite: implication of the Fe3+ AlO3 substitution in MgSiO3 perovskite at the lower mantle condition.
488   *Geophysical Research Letters, 32*(16).
489 Okuda, Y., Ohta, K., Sinmyo, R., Hirose, K., Yagi, T., & Ohishi, Y. (2019). Effect of spin transition of iron on the
490   thermal conductivity of (Fe, Al)-bearing bridgmanite. *Earth and Planetary Science Letters, 520*, 188-198.
491 Potapkin, V., McCammon, C., Glazyrin, K., Kantor, A., Kupenko, I., Prescher, C., et al. (2013). Effect of iron
492   oxidation state on the electrical conductivity of the Earth's lower mantle. *Nature communications, 4*, 1427.
493 Prakapenka, V., Kubo, A., Kuznetsov, A., Laskin, A., Shkurikhin, O., Dera, P., et al. (2008). Advanced flat top laser
494   heating system for high pressure research at GSECARS: application to the melting behavior of germanium.
495   *High Pressure Research, 28*(3), 225-235.
496 Prescher, C., & Prakapenka, V. B. (2015). DIOPTAS: a program for reduction of two-dimensional X-ray diffraction
497   data and data exploration. *High Pressure Research, 35*(3), 223-230.
498 Ross, N. L., Ko, J., & Prewitt, C. T. (1989). A new phase transition in MnTiO 3: LiNbO 3-perovskite structure.
499   *Physics and Chemistry of Minerals, 16*(7), 621-629.
500 Rustad, J. R., & Yin, Q.-Z. (2009). Iron isotope fractionation in the Earth's lower mantle. *Nature Geoscience, 2*(7),
501   514.
502 Seto, Y., Nishio-Hamane, D., Nagai, T., & Sata, N. (2010). Development of a software suite on X-ray diffraction
503   experiments. *Review of High Pressure Science and Technology, 20*(3).
504 Shannon, R. D. (1976). Revised effective ionic radii and systematic studies of interatomic distances in halides and
505   chalcogenides. *Acta crystallographica section A: crystal physics, diffraction, theoretical and general
506   crystallography, 32*(5), 751-767.
507 Sinmyo, R., Pesce, G., Greenberg, E., McCammon, C., & Dubrovinsky, L. (2014). Lower mantle electrical
508   conductivity based on measurements of Al, Fe-bearing perovskite under lower mantle conditions. *Earth
509   and Planetary Science Letters, 393*, 165-172.
510 Sturhahn, W. (2000). CONUSS and PHOENIX: Evaluation of nuclear resonant scattering data. *Hyperfine
511   Interactions, 125*(1-4), 149-172.
512 Toby, B. H. (2001). EXPGUI, a graphical user interface for GSAS. *Journal of applied crystallography, 34*(2), 210-
513   213.
514 Tschauner, O., Ma, C., Beckett, J. R., Prescher, C., Prakapenka, V. B., & Rossman, G. R. (2014). Discovery of
515   bridgmanite, the most abundant mineral in Earth, in a shocked meteorite. *Science, 346*(6213), 1100-1102.
516 Wang, X., Tsuchiya, T., & Hase, A. (2015). Computational support for a pyrolitic lower mantle containing ferric
517   iron. *Nature Geoscience, 8*(7), 556.
518 Wechsler, B. A., & Prewitt, C. T. (1984). Crystal structure of ilmenite (FeTiO3) at high temperature and at high
519   pressure. *American Mineralogist, 69*(1-2), 176-185.
520 Yim, W., & Paff, R. (1974). Thermal expansion of AlN, sapphire, and silicon. *Journal of Applied Physics, 45*(3),
521   1456-1457.

522

Author Manuscript

Figure captions

Figure 1. X-ray diffraction patterns of compressed FA50 polymorphs at 300 K. (a) LiNbO$_3$-type (LN) FA50 at 1.3 GPa, 300 K with $a = 4.864(1)$ Å and $c = 12.997(3)$ Å; (b) FA50 bridgmanite (Bdg) at 102.2 GPa, 300 K after laser annealing with $a = 4.385(6)$ Å, $b = 4.690(3)$ Å and $c = 6.410(13)$ Å. Ticks of gold (Au), neon (Ne) and the residual curve (blue) between experimental data (black cross) and fitted curve (red line) are shown.
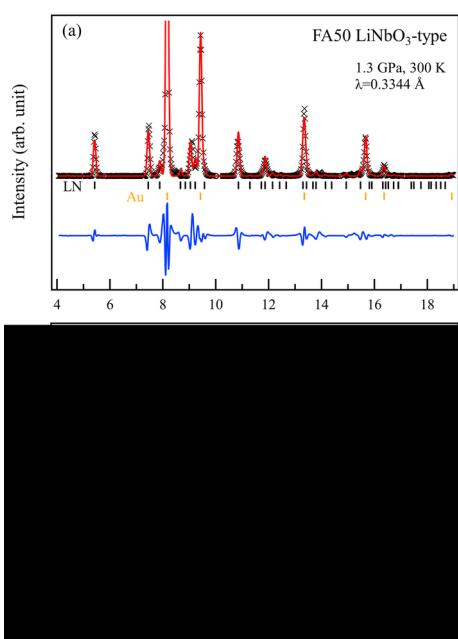
Figure 2. Comparison of internal energy of different cation orderings in FA50 bridgmanite. All structures are calculated at fixed volume of 167.53 Å^3. The most energetically favored structure (No. 4, black filled square) and two close competitors (No. 3 & 6, gray filled squares) share the same type of B-site ordering, in which each Si atom (dark blue spheres and octahedra) is bridged to six Al atoms (light blue spheres and octahedra) by O atoms (red spheres), and vice versa. Structure No. 4 has an alternating Mg (light brown spheres) and Fe (dark brown spheres) sheet arrangement in ac (010) plane along the b axis direction. This indicates that the Fe and Al atoms alternate between the closest neighbor sites along the (110) and (1-10) plane normal directions but align separately in column in the (001) plane normal direction.

Figure 3. Compression curve of FA50 bridgmanite at 300 K. (a) Unit-cell volume as a function of pressure. Sample 1 (filled squares) was laser-annealed after each compression, while sample 2 (open circles) was cold compressed to the highest pressure. (b) Normalized stress – Eulerian strain (F-f) plot. Symbols correspond to those in (a). The data can be fitted linearly with slope close to 0, indicating the validity of using a 2nd order BM-EoS.

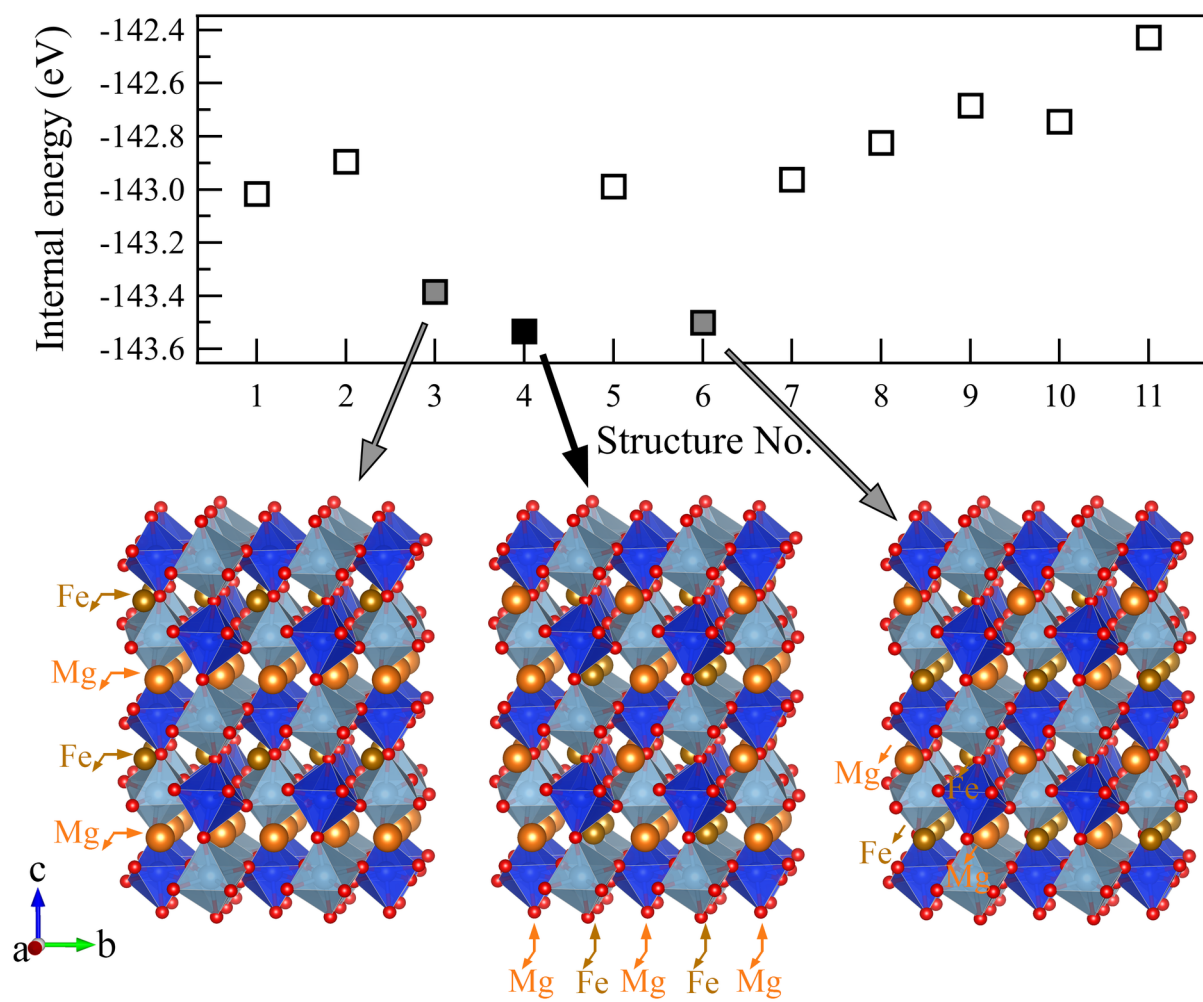**Figure 4. X-ray emission spectroscopy measurements of FA50 bridgmanite at high pressures.** (a) XES Fe K_β spectra of FA50 from 18 to 80 GPa, together with the LS (black dotted) reference spectra. The spectra at 18 GPa (black solid) was used as HS reference. All spectra were normalized to unity in integral area and aligned by the position of the K_β main peak. Inset: Fe K_β satellite peak, whose area shrank after laser heating at high pressure, indicating a decrease of HS Fe^{3+} species. (b) The HS fraction of Fe^{3+} calculated by the IAD of the Fe K_β satellite peak (open circles). The IAD method integrates the satellite peak area to the isobestic point around 7049 eV; For comparison, the IRD method (filled squares) integrates the area at 7030-7056 eV, to correct for natural peak broadening at high pressure.

Figure 5. SMS measurements of compressed FA50 bridgmanite after laser heating. At 35 GPa the spectrum can be fitted by one Fe site, which corresponds to the HS Fe^{3+} at the A site. Fitting the spectrum at 80 GPa requires at least two Fe sites: 69% Fe^{3+} with a low quadrupole splitting (QS) was assigned to a HS-state, and 31% Fe^{3+} with a high QS was assigned to a LS-state (Lin et al., 2012; Liu et al., 2018). The difference in center shift (ΔC) between the two sites is 0.22 mm/s, consistent with the 0.1-0.3 mm/s values for FF50 sample (Liu et al., 2018). The SMS measurements were done on the same sample in XES measurements.
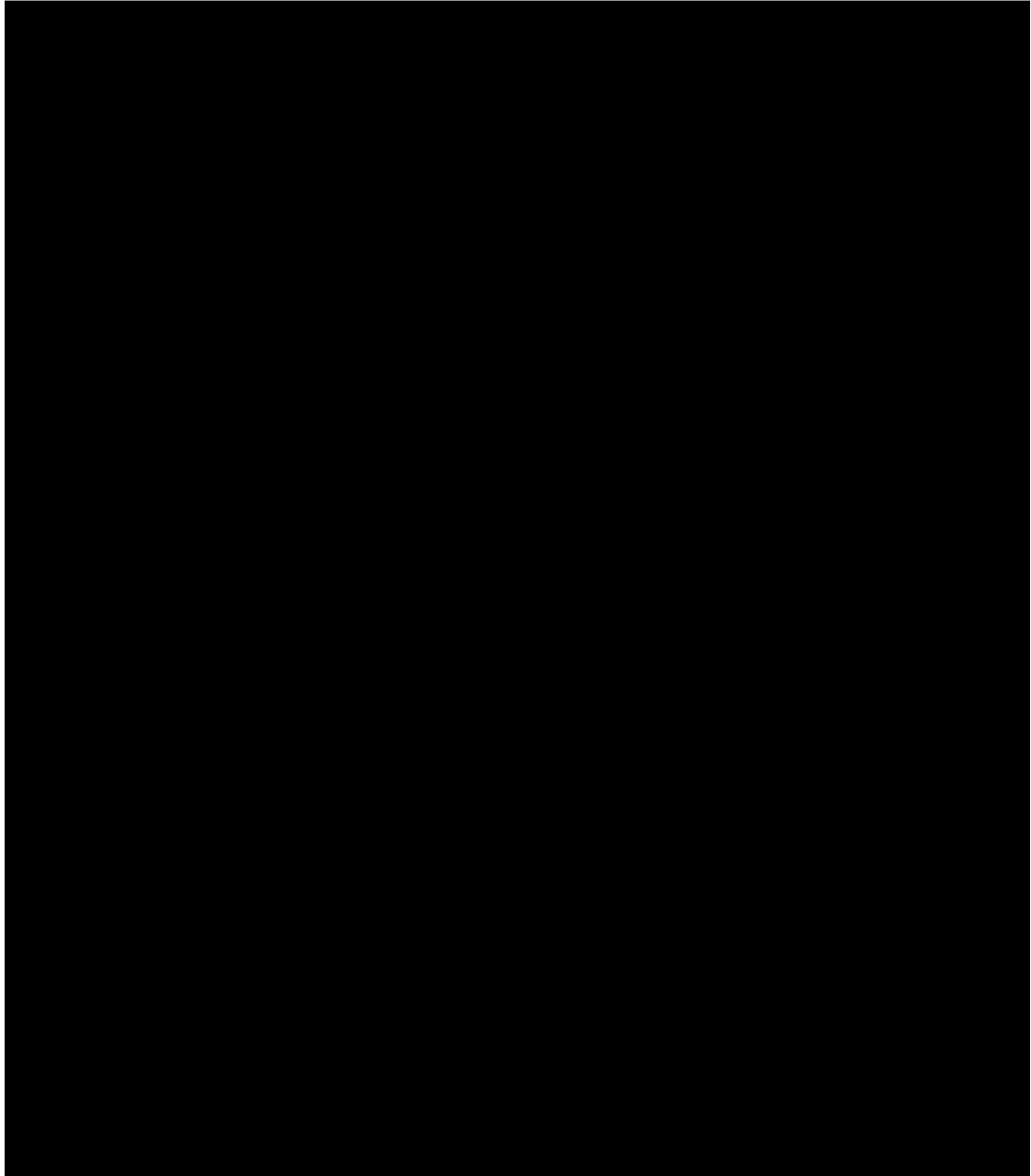
Figure 6. Calculated bulk sound velocity of FA50 bridgmanite. The bulk sound velocity shows a negative correlation with its Fe^{3+}content, mainly because the atomic mass of Fe is about twice as heavy as that of Mg, Al, or Si. At 130 GPa and 300 K, the bulk sound velocity of MgSiO$_3$ is 7.7% higher than that of FA50 bridgmanite (50% Fe^{3+} in A site), which in turn is 8.7% higher than that of FF50 bridgmanite (additional 50% Fe^{3+} in B site).
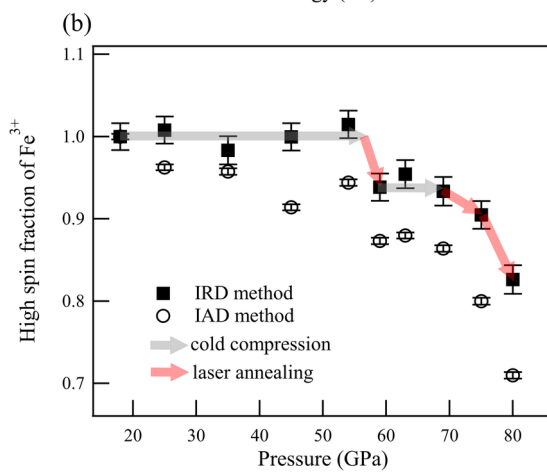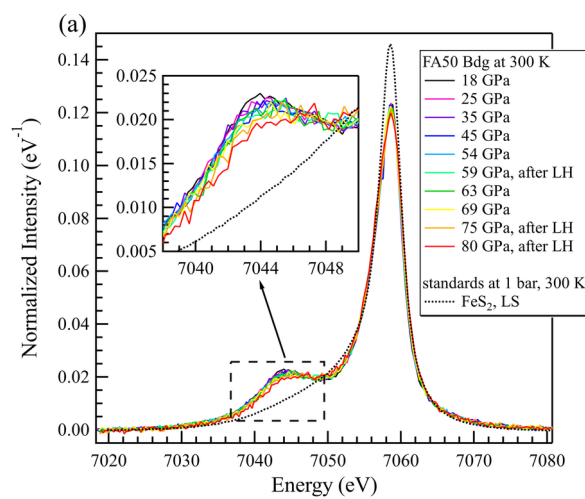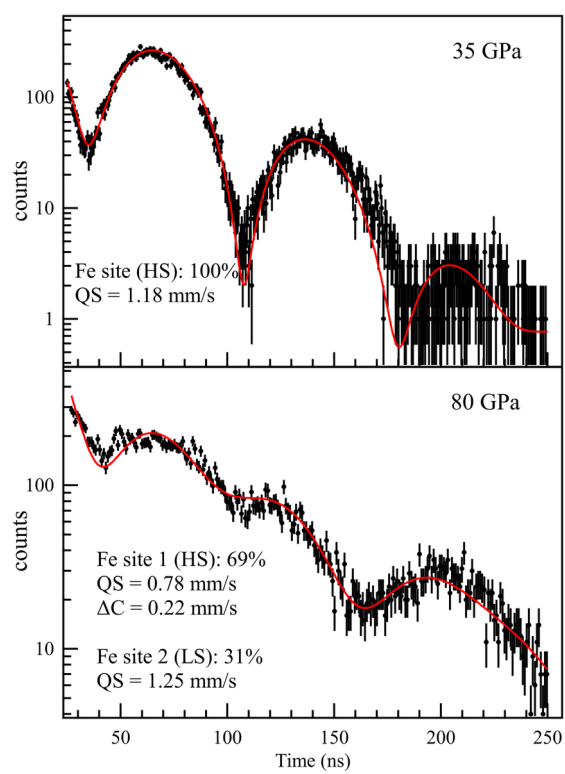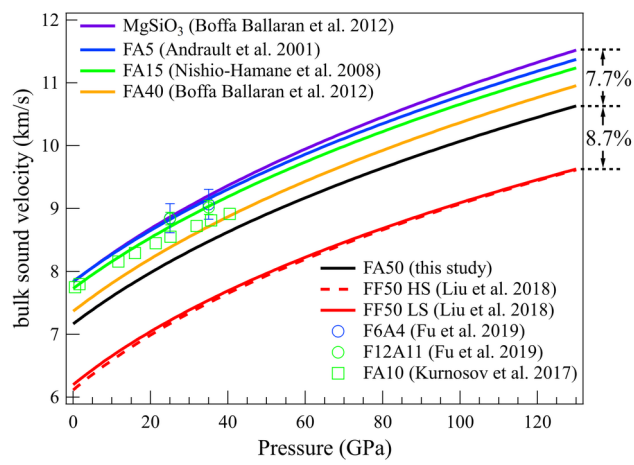
2020JB019964-f01-z-.tif

2020JB019964-f02-z-.tif

2020JB019964-f03-z-.tif

(a) FA50 Bdg at 300 K
— 18 GPa
— 25 GPa
— 35 GPa
— 45 GPa
— 54 GPa
— 59 GPa, after LH
— 63 GPa
— 69 GPa
— 75 GPa, after LH
— 80 GPa, after LH

standards at 1 bar, 300 K
····· FeS_2, LS

(b)
- IRD method
○ IAD method
→ cold compression
→ laser annealing

2020JB019964-f04-z-.tif

2020JB019964-f05-z-.tif

2020JB019964-f06-z-.tif